
This is an electronic reprint of the original article.
This reprint may differ from the original in pagination and typographic detail.

Behrends, Jan; Grushin, Adolfo G.; Ojanen, Teemu; Bardarson, Jens H.

Visualizing the chiral anomaly in Dirac and Weyl semimetals with photoemission spectroscopy

Published in:
Physical Review B

DOI:
[10.1103/PhysRevB.93.075114](https://doi.org/10.1103/PhysRevB.93.075114)

Published: 08/02/2016

Document Version
Publisher's PDF, also known as Version of record

Please cite the original version:
Behrends, J., Grushin, A. G., Ojanen, T., & Bardarson, J. H. (2016). Visualizing the chiral anomaly in Dirac and Weyl semimetals with photoemission spectroscopy. *Physical Review B*, 93(7), Article 075114.
<https://doi.org/10.1103/PhysRevB.93.075114>

This material is protected by copyright and other intellectual property rights, and duplication or sale of all or part of any of the repository collections is not permitted, except that material may be duplicated by you for your research use or educational purposes in electronic or print form. You must obtain permission for any other use. Electronic or print copies may not be offered, whether for sale or otherwise to anyone who is not an authorised user.

Visualizing the chiral anomaly in Dirac and Weyl semimetals with photoemission spectroscopyJan Behrends,¹ Adolfo G. Grushin,¹ Teemu Ojanen,² and Jens H. Bardarson¹¹*Max-Planck-Institut für Physik komplexer Systeme, Nöthnitzer Str. 38, 01187 Dresden, Germany*²*Low Temperature Laboratory, Department of Applied Physics, Aalto University, FI-00076 AALTO, Finland*

(Received 23 September 2015; revised manuscript received 20 January 2016; published 8 February 2016)

Quantum anomalies are the breaking of a classical symmetry by quantum fluctuations. They dictate how physical systems of diverse nature, ranging from fundamental particles to crystalline materials, respond topologically to external perturbations, insensitive to local details. The anomaly paradigm was triggered by the discovery of the chiral anomaly that contributes to the decay of pions into photons and influences the motion of superfluid vortices in ³He-A. In the solid state, it also fundamentally affects the properties of topological Weyl and Dirac semimetals, recently realized experimentally. In this work we propose that the most identifying consequence of the chiral anomaly, the charge density imbalance between fermions of different chirality induced by nonorthogonal electric and magnetic fields, can be directly observed in these materials with the existing technology of photoemission spectroscopy. With angle resolution, the chiral anomaly is identified by a characteristic note-shaped pattern of the emission spectra, originating from the imbalanced occupation of the bulk states and a previously unreported momentum dependent energy shift of the surface state Fermi arcs. We further demonstrate that the chiral anomaly likewise leaves an imprint in angle averaged emission spectra, facilitating its experimental detection. Thereby, our work provides essential theoretical input to foster the direct visualization of the chiral anomaly in condensed matter, in contrast to transport properties, such as negative magnetoresistance, which can also be obtained in the absence of a chiral anomaly.

DOI: [10.1103/PhysRevB.93.075114](https://doi.org/10.1103/PhysRevB.93.075114)**I. INTRODUCTION**

Quantum anomalies occur when a classically preserved symmetry is broken upon quantization [1]. The chiral anomaly, the first known example, refers to the nonconservation of a chiral current—a current imbalance between two distinct species of chiral fermions. Its discovery resolved the discrepancy between the measured and calculated decay rate of the neutral pion into two photons [1], and in condensed matter it was first identified as being responsible for a transverse force acting on vortices in superfluid ³He-A [2,3]. In the solid state, Weyl and Dirac semimetals are described at low energies by chiral fermions that realize a chiral anomaly and host topological surface states with Fermi arcs [4,5]. TaAs was recently theoretically predicted [6,7] and experimentally identified using angle-resolved photoemission spectroscopy [8,9] (ARPES) as being a Weyl semimetal, with Na₃Bi [10–13], Cd₃As₂ [14–20], and ZrTe₅ [21] likewise identified as Dirac semimetal. Rapidly other materials in the TaAs class were also shown to be Weyl semimetals [22–24]. In this work we theoretically explore the spectroscopic signatures of the chiral anomaly in these materials, with special emphasis on its effect on the Fermi arcs. We reveal an identifying note-shaped structure obtained in ARPES and a characteristic peaked structure of angular averaged photoemission spectra that allow for an experimental visualization of the chiral anomaly.

Weyl semimetals are a topological state of matter in which the conduction and valence bands touch and linearly disperse around pairs of Weyl nodes [4,5]. Each node has a definite left or right handed chirality providing a quantum number analogous to the valley degree of freedom in graphene [25]. Dirac semimetals can be thought of as two superimposed copies of Weyl semimetals with the degeneracy protected by a crystal symmetry from opening up a gap [6,7,26–28]. Similar to topological insulators and their metallic surface,

Dirac and Weyl semimetals host protected surface states [29] that unconventionally only exist for a restricted range of crystal momenta, thereby forming a Fermi arc connecting a pair of Weyl points with opposite chirality [29,30]. Fermi arcs have been identified with ARPES in both TaAs [8,9] and Na₃Bi [13].

The chiral fermions describing the low energy degrees of freedom of Dirac and Weyl semimetals exhibit the chiral anomaly [31–33]: while the sum of left and right handed fermions is necessarily conserved, their difference, the chiral density, does not have to be, even if classically it should. In fact, nonorthogonal magnetic and electric fields pump left handed fermions into right handed, or vice versa [32–37]. Disorder induced internode scattering eventually counterbalances the pumping, leading to a nonequilibrium steady state with a nonzero chiral density. The chiral anomaly is theoretically predicted to result in negative magnetoresistance [38,39] (consistent with recent magnetotransport experiments [21,40–48]), local [49,50] and nonlocal [51] transport phenomena, chiral optical activity [35,52,53], and rotation induced cooling [54].

A clean diagnostic tool for the chiral anomaly is still lacking, since transport signatures, such as negative magnetoresistance, are not as unequivocal as initially believed [55,56]. Photoemission spectroscopy (PES) has previously been overlooked in this regard despite its importance in observing topological semimetals. A possible reason for this is that the finite magnetic field required to observe the chiral anomaly may complicate the disentangling of electron trajectories needed for angular resolution. Setting aside this obstacle (we return to it at the end of this work where we argue that it can be overcome) we identify the main spectral signatures of the chiral anomaly and its observable effect on the Fermi arcs. First, the bulk spectrum is determined by the differently occupied Weyl nodes distinguished by their chiralities; second, the bulk chiral imbalance tilts the Fermi arcs, which then appear at fixed energy as finite segments stemming from the bulk Fermi

surface. Together, these two features form a distinguishing note-shaped photoemission pattern that we argue are within reach of current experimental state of the art. We further calculate angle integrated PES, which does not suffer from the magnetic field complications of its ARPES relative, and show that distinct signatures of the chiral anomaly survive. Overall, our results supply essential theoretical input that render photoemission spectroscopy a viable probe to visualize the chiral anomaly in Dirac and Weyl semimetals.

II. VISUALIZING THE CHIRAL ANOMALY WITH ARPES AND PES

A. Background and summary of main results

To support our conclusions, we start by discussing the main features of the band structure of Weyl semimetals, shown in Fig. 1(a). Their low-energy bulk spectrum consists of an even number of band touching points of left (L) and right (R) handed chirality that are separated in energy and momentum by breaking inversion or time-reversal symmetry. Close to the Weyl points the energy dispersion is approximately linear and described by a Weyl Hamiltonian

$$\mathcal{H}_{L/R} = \pm \hbar v \boldsymbol{\sigma} \cdot \mathbf{k}, \quad (1)$$

with \mathbf{k} the momentum, $\boldsymbol{\sigma}$ the vector of Pauli matrices, and v the Fermi velocity. Its eigenstates have a spin that points either radially away from or into the Weyl point, depending on its chirality. Each Weyl node therefore acts as a monopole of Berry flux in momentum space [3,57]. In analogy with

magnetic monopoles, a Dirac string necessarily emanates from the monopoles connecting a pair with opposite chirality [58]. Any two dimensional plane in momentum space, spanned say by the two momenta k_x and k_y at a fixed k_z , that crosses the Dirac string an odd number of times and does not contain a Weyl point defines a topologically nontrivial gapped band structure. Therefore, if the system is made into a film that is finite in a real space direction conjugate to a momentum in that plane, for example either the x or y direction, a chiral surface state is obtained at the corresponding surfaces [29]. Since k_z remains a good quantum number we can repeat this argument for different planes at different k_z . Only those crossing the Dirac string odd times have a surface state, which therefore only exists for certain values of the k_z momenta. The surface state dispersion is depicted as the gray shaded plane leaning on the two Weyl nodes in Fig. 1(a) (the opposite surface provides an analogous surface plane with opposite velocity that is not shown). The separator between occupied and unoccupied surface states is an arc—the Fermi arc.

In the presence of nonorthogonal external electric (\mathbf{E}) and magnetic (\mathbf{B}) fields, the chiral anomaly leads to a nonconservation of the left and right handed electron densities. This is expressed by the two coupled continuity equations

$$e \partial_t n_{L/R} + \nabla \cdot \mathbf{j}_{L/R} = \mp \frac{e^3}{4\pi^2 \hbar^2} \mathbf{E} \cdot \mathbf{B} \pm \frac{e}{2\tau_v} (n_R - n_L), \quad (2)$$

where $n_{L/R}$ is the density of left and right handed fermions measured from the Weyl point and $\mathbf{j}_{L/R}$ their current density. The first term on the right hand side is the anomaly

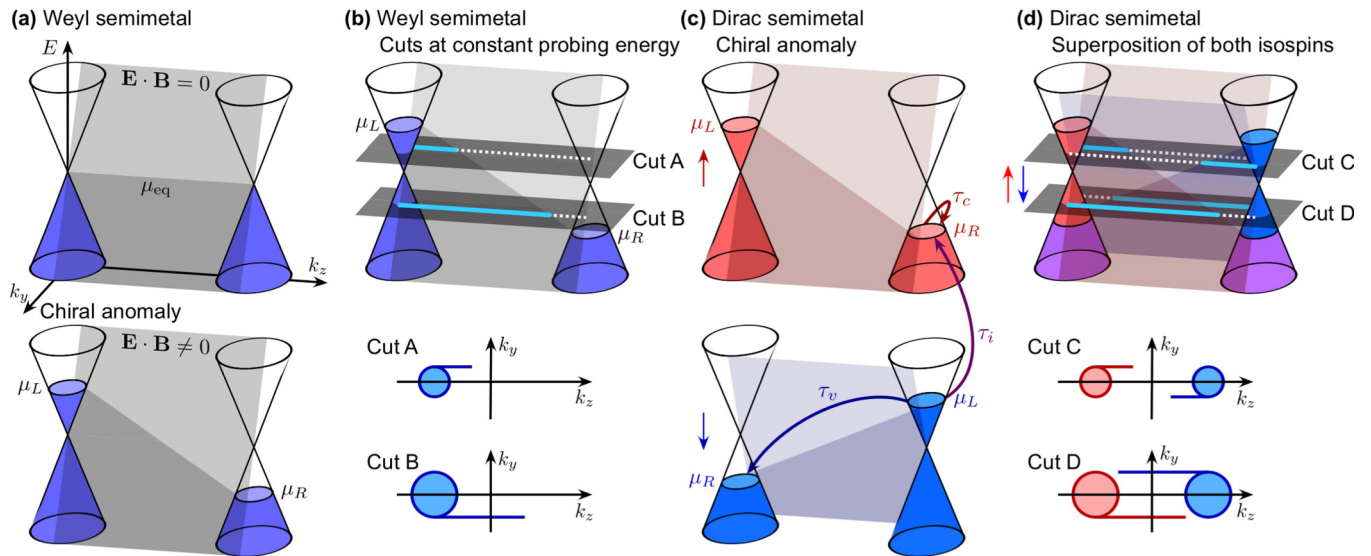


FIG. 1. Visualization of the chiral anomaly in Dirac and Weyl semimetals. (a) Low-energy spectrum of a Weyl semimetal film with two bulk Weyl nodes of different chirality separated in momentum space. The gray plane represents the surface state at the film's top surface, occupied up to the equilibrium chemical potential μ_{eq} . Applying external magnetic and electric fields that satisfy $\mathbf{E} \cdot \mathbf{B} \neq 0$ results in a steady state with left and right cone chemical potentials $\mu_L \neq \mu_R$, linearly interpolated by a tilted Fermi arc. (b) Two constant energy cuts (A and B) through the band structure, with occupied and empty surface states depicted by solid light blue and white dashed lines, respectively. The occupation at these cuts shows a characteristic blue note-shaped pattern depicted in the lower panel. (c) Dirac semimetals host pairs of Weyl cones, each pair with fixed isospin (\uparrow or \downarrow) and both left and right chiralities, that respond to the chiral anomaly in the opposite way. Two edge states with opposite velocities (light red and light blue planes) appear at each boundary of the Dirac semimetal. Scattering processes within and between cones with scattering times τ_c , τ_v , and τ_i are depicted by arrows. (d) The two pairs of Weyl nodes in (c) together comprise a pair of Dirac nodes. At fixed energy cuts (C and D) between μ_L and μ_R , both bulk nodes are occupied while the surface states are only partially occupied. The total occupation in these planes describes two facing note-shaped patterns, illustrated in the bottom panel.

contribution, which has a different sign for the two chiralities; the second term represents the intervalley scattering with rate τ_v^{-1} . At long times, a steady state with occupation difference between the two chiralities is obtained. The continuity equations (2) and particle conservation then define the left and right handed chemical potentials

$$\mu_{L/R} = \left[\mu_{\text{eq}}^3 \mp \frac{3}{2} \hbar v^3 e^2 \tau_v \mathbf{E} \cdot \mathbf{B} \right]^{1/3}, \quad (3)$$

where μ_{eq} is the equilibrium chemical potential and we have used that $n_{L/R} = \mu_{L/R}^3 / (6\pi^2 \hbar^3 v^3)$ for three dimensional Weyl fermions. In defining $\mu_{L/R}$ we assume that the equilibration [59] within a node with intravalley relaxation time τ_c is much shorter than the intervalley equilibration time τ_v [51]. This similarly suggests that relaxation along the surfaces is dominated by small momentum scattering such that the Fermi arc linearly interpolates in momentum space between μ_L and μ_R , analogous to the voltage drop along an ohmic wire, leading to the steady-state occupation shown in the bottom of Fig. 1(a). At a fixed energy between μ_R and μ_L this results in the characteristic note-shaped occupation schematically shown in Fig. 1(b) for the two constant energy planes denoted cut A and cut B.

Dirac semimetals can be understood as two copies of Weyl semimetals, with each Dirac node composed of two Weyl fermions of opposite chirality. The two copies are distinguished by their different total angular momentum [28], which can be captured by an isospin quantum number that we denote with \uparrow and \downarrow . As long as the crystal symmetry is not broken, the isospin remains a good quantum number. This has two important consequences: one, the two chiral fermions comprising a Dirac node are decoupled and therefore a gap does not open; two, the Weyl nodes still act as monopoles in momentum space and their Dirac string connects monopoles with opposite chirality but the *same* isospin. Dirac semimetals therefore have two Fermi arcs with opposite velocity on each surface.

The two pairs of Weyl fermions in the Dirac semimetal are oppositely affected by the chiral anomaly. External and nonorthogonal \mathbf{E} and \mathbf{B} fields shift the occupation in one Dirac cone to higher energies for one isospin and to lower for the other, and oppositely in the other Dirac cone, as schematically shown in Fig. 1(c). For this steady state to be realized, intravalley relaxation at fixed chirality must be larger than both the intervalley relaxation, $\tau_c^{-1} \gg \tau_v^{-1}$, and the intravalley relaxation between isospins, $\tau_c^{-1} \gg \tau_i^{-1}$ [the different relaxation processes are depicted with arrows in Fig. 1(c)]. Both conditions are estimated to be satisfied in Dirac semimetals [51]. Moreover, high mobility materials such as graphene satisfy the condition $\tau_c^{-1} \gg \tau_v^{-1}$, which allows for the experimental observation of a chemical potential imbalance [60] and suggests that it is also met in Cd_3As_2 .

The total occupation of a given Dirac cone is a superposition of both isospins, and therefore the bulk occupation in the chiral anomaly induced steady state is qualitatively the same as in its absence: two circular disks. In contrast, the tilt of the Fermi arcs and the resulting partial occupation at a fixed energy, see Fig. 1(d), leads to a qualitatively new signature in the form of two facing note-shaped patterns (familiar from the Weyl semimetal case). This key property, which allows

photoemission of Dirac semimetals to show evidence of the chiral anomaly, is a central result of our work.

B. Model and methods

We establish by a numerical computation that these note-shaped patterns are indeed directly manifested in photoemission spectra. Our simulated data is obtained with exact diagonalization of tight binding models of Weyl and Dirac semimetals. For a Weyl semimetal we take

$$H_{\text{WSM}} = H_0 + H_1, \quad (4a)$$

$$H_0 = 2v(\sin k_y \sigma_x - \sin k_x \sigma_y) \tau_z + 2v_z \sin k_z \tau_y + M_{\mathbf{k}} \tau_x, \quad (4b)$$

$$H_1 = b_0 \sigma_z \tau_y + \mathbf{b} \cdot (-\sigma_x \tau_x, \sigma_y \tau_x, \sigma_z). \quad (4c)$$

The first term (H_0) models a three-dimensional topological insulator [61]. The Pauli matrices σ and τ respectively act in spin and particle-hole space. The velocity v in the x and y directions differs from that in the z direction (v_z) consistent with experimentally relevant materials and $M_{\mathbf{k}} = \epsilon - 2t \sum_i \cos k_i$. At $\epsilon = 6t$ a degenerate three-dimensional Dirac cone is obtained at $\mathbf{k} = 0$. The second term [62] (H_1) breaks inversion with a nonzero b_0 and time-reversal symmetry with a finite \mathbf{b} . In our simulation we take $b_0 = 0$ and fix the direction of $\mathbf{b} = (0, 0, b_z)$ such that the Dirac cone is split into two Weyl cones at $k_z \approx \pm b_z / (2v_z)$.

The low-energy spectrum of both Dirac semimetals Na_3Bi [27] and Cd_3As_2 [28] is modeled by the Hamiltonian

$$H_{\text{DSM}} = M_{\mathbf{k}} \sigma_z + 2v(\sin k_x \sigma_x \tau_z - \sin k_y \sigma_y), \quad (5)$$

which can be understood as two copies of two-band Weyl semimetal Hamiltonians. The mass term $M_{\mathbf{k}} = M_0 + 2M_1(\cos k_z - 1) + 2M_2(\cos k_x + \cos k_y - 2)$ sets the velocity in k_z direction to $v_z = 2\sqrt{M_0 M_1}$ and the Dirac cones to be at $k_z^c = \pm \sqrt{M_0 / M_1}$.

To model a film we take the system finite in the direction orthogonal to the separation of the cones in momentum space, which is the surface where the edge states are maximally visible. The ARPES spectrum is given by an integral over the local density of states

$$I(\mathbf{k}_{\parallel}, \omega) = \int dx \sum_n |\psi_{n, \mathbf{k}_{\parallel}}(x)|^2 \delta(\epsilon_{n, \mathbf{k}_{\parallel}} - \omega) w(x) f(\omega - \mu_{\mathbf{k}_{\parallel}}), \quad (6)$$

where x is the coordinate in the finite direction of the film, $w(x) = \exp(-x/\ell)$ is a weight function modeling the incoming light's intensity decay with depth into the sample with decay length ℓ , and f is the Fermi-Dirac distribution. The wave functions $\psi_{n, \mathbf{k}_{\parallel}}$ are the eigenfunctions of the Hamiltonians and $\epsilon_{n, \mathbf{k}_{\parallel}}$ the corresponding eigenvalues, which depend on the momentum \mathbf{k}_{\parallel} parallel to the surface. To model the chiral anomaly induced steady state, the chemical potential $\mu_{\mathbf{k}_{\parallel}}$ is taken to be \mathbf{k}_{\parallel} and isospin dependent. For the surface states, $\mu_{\mathbf{k}_{\parallel}}$ depends linearly on k_z .

C. ARPES spectra for Weyl and Dirac semimetals

In Fig. 2(a) we plot the momentum resolved ARPES spectra at various fixed energies for a doped Weyl semimetal in

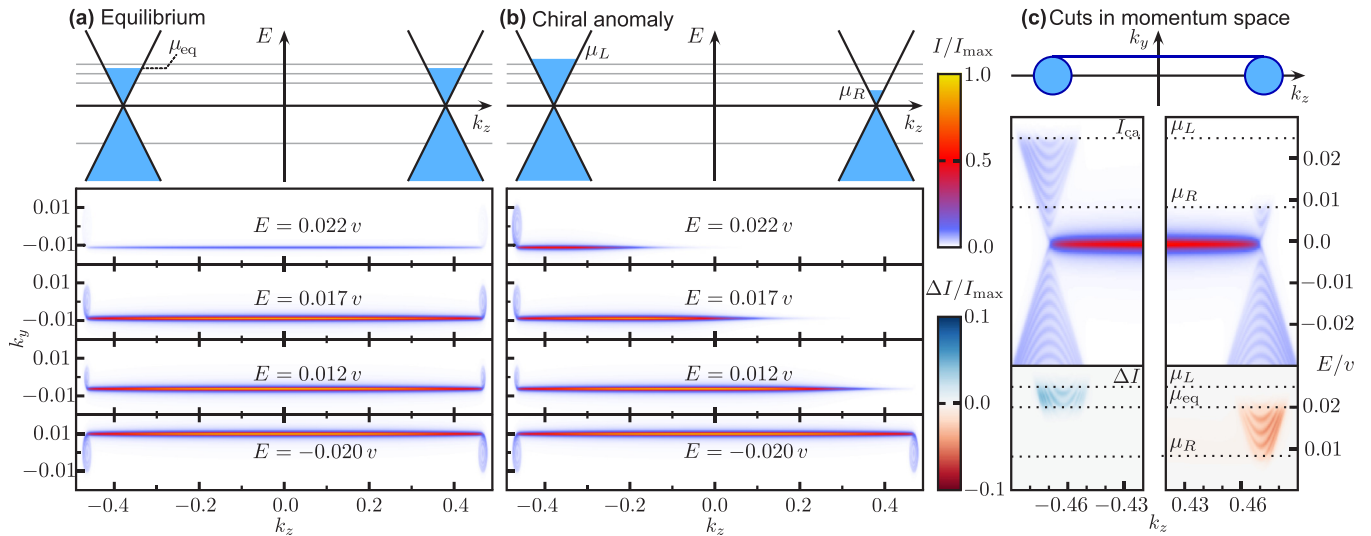


FIG. 2. ARPES signatures of the chiral anomaly in Weyl semimetals. Numerically computed ARPES spectra for a doped Weyl semimetal film with $L = 2000$ layers in (a) equilibrium and (b) and (c) the chiral anomaly induced steady state. The parameters are such that the equilibrium chemical potential is $\mu_{\text{eq}} = 0.02v$ while in nonequilibrium the left and right cones are filled up to $\mu_L = 0.025v$ and $\mu_R = 0.008v$, respectively. The lower panels in (a) and (b) show the momentum resolved spectra at a fixed energy, located as schematically shown with gray lines in the upper panels. In equilibrium (a), bulk cones and the surface state are observed, while the chiral anomaly (b) results in the disappearance of one cone and the emerging of the characteristic note-shaped pattern between μ_L and μ_R . The panel (c) shows the ARPES spectrum in nonequilibrium at a fixed $k_y = 0$, depicted in the top panel. The upper plot in the lower panel shows the total ARPES spectra, demonstrating the conelike structure from the bulk and the flat surface state; the lower plot displays the intensity difference $\Delta I = I_{\text{ca}} - I_{\text{eq}}$ between the out-of-equilibrium and the equilibrium states. The dashed lines mark the chemical potentials μ_L, μ_R , and μ_{eq} . These plots were obtained for $v = v_z, t = 0.5v, \epsilon = 6t$, and $b_z = 0.9v$ with the temperature set to $T = 0.001v$, which corresponds to $T \approx 5$ K for a typical Fermi velocity of $v = 0.45$ eV (see Sec. II B and the Appendix A for details).

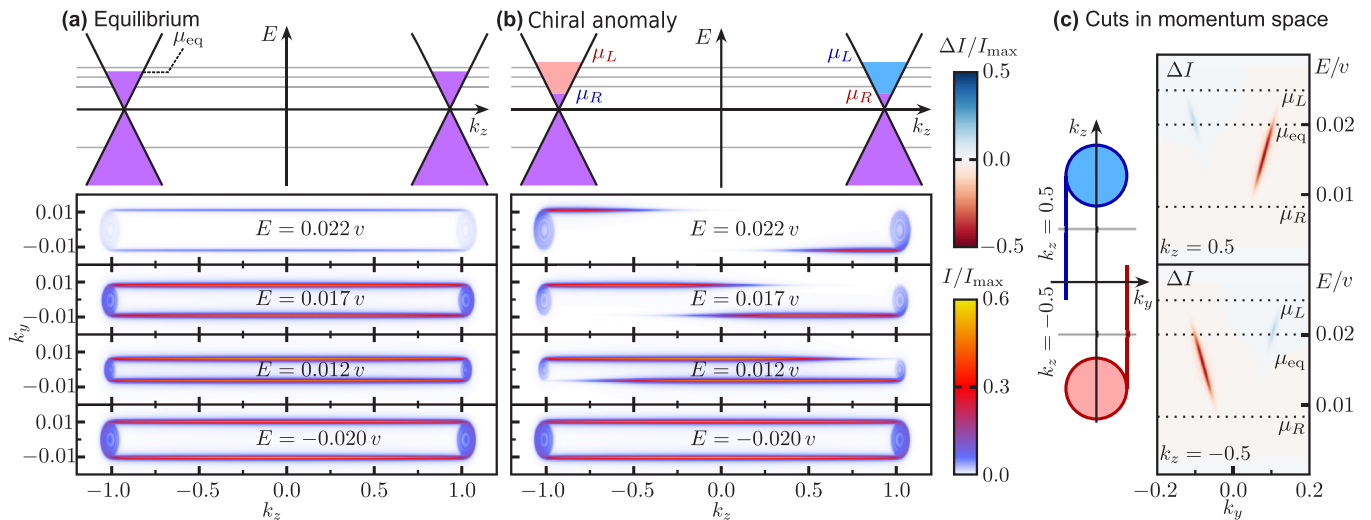


FIG. 3. ARPES signatures of the chiral anomaly in Dirac semimetals. Numerically computed ARPES spectra for a doped Dirac semimetal film of $L = 2000$ layers in (a) equilibrium and (b) and (c) the presence of $\mathbf{E} \cdot \mathbf{B} \neq 0$. The spectra in (a) and (b) are the momentum resolved spectra at the fixed energies schematically shown at the top as gray lines. The equilibrium chemical potential is set to $\mu_{\text{eq}} = 0.020v$, while the left and right out-of-equilibrium chemical potentials are chosen to be $\mu_L = 0.025v$ and $\mu_R = 0.008v$. While there is a slight bulk Dirac cone intensity reduction from the equilibrium to the nonequilibrium situation, a stark qualitative difference is observed in the surface states that leads to the characteristic double note-shaped pattern. In (c) we plot the intensity difference $\Delta I = I_{\text{ca}} - I_{\text{eq}}$ for a fixed momentum $k_z = \pm 0.5$, which reveals the linear dispersion of the edge state. These plots were obtained for $M_0 = -0.2v, M_1 = -0.25v, M_2 = -0.75v$, and a temperature of $T = 0.001v$. With $v = 0.45$ eV for Na_3Bi , the temperature corresponds to $T \approx 5$ K and the induced chemical potential difference to $\delta\mu \approx 8$ meV.

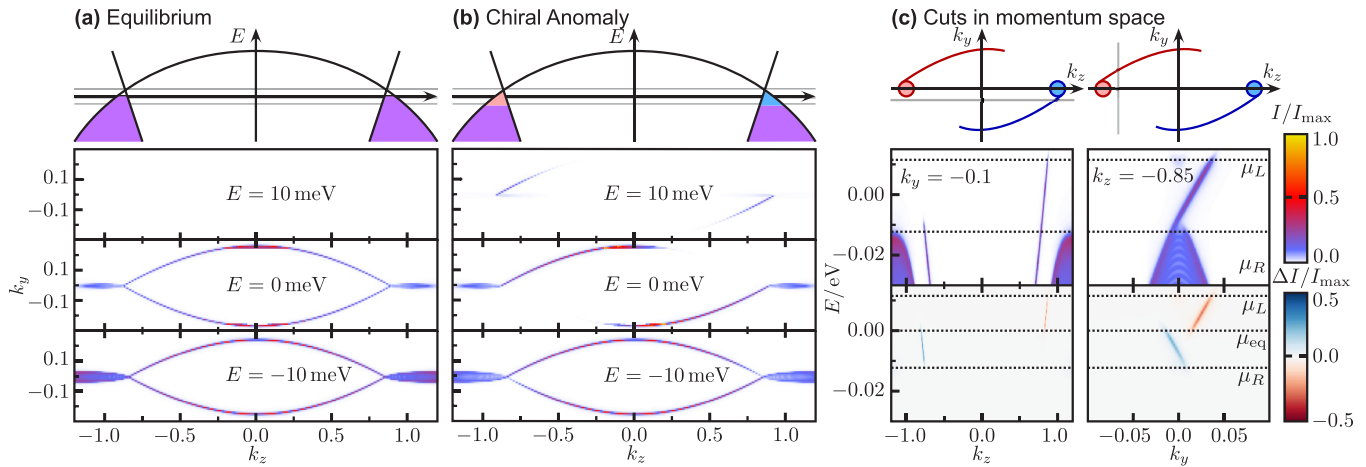


FIG. 4. Visualization of the chiral anomaly in Na₃Bi. (a) Numerically computed equilibrium ARPES spectra for a doped Dirac semimetal film Na₃Bi with $\mu_{\text{eq}} = 0$. The pair of Fermi arcs are well within experimental energy and momentum resolution, confirmed by the recent experiment in Ref. [13]. (b) Chiral anomaly induced ARPES spectra for the same material and an estimate of the chiral chemical potential difference $\delta\mu \approx 20$ meV derived in section A. The Fermi arcs show evidence of partial occupation within experimental resolution. The upper panels in (a) and (b) show a schematic representation of the bulk band structure with two Dirac nodes connected at higher energies. (c) The lower panel shows two cuts through momentum space at $k_y = -0.1$ and $k_z = -0.85$ in units of the lattice constants and represented schematically by the horizontal and vertical light gray lines in the upper panel. The parameters of the low energy model used to obtain these figures are extracted from first principles in Ref. [27] and take the values $v = 0.45$ eV, $M_0 = -0.087$ eV, $M_1 = -0.11$ eV, $M_2 = -0.35$ eV and $C_0 = -0.064$ eV, $C_1 = 0.094$ eV, $C_2 = -0.28$ eV. All calculations were performed at a temperature of $T = 1$ meV = 11.6 K and for a film thickness of $L = 1000$ layers.

equilibrium. Two bulk cones and one surface state at the probed surface are clearly seen; the surface state localized at the opposite surface is not visible due to the finite penetration depth of the incoming photon. In the presence of external fields $\mathbf{E} \cdot \mathbf{B} \neq 0$, the note-shaped pattern of the occupied states is seen in Fig. 2(b) for energies between μ_L and μ_R . An alternative way to illustrate the steady state occupation with $\mu_R \neq \mu_L$ is through a cut in momentum space at a fixed $k_y = 0$ as provided in Fig. 2(c). The pumping of charge between the different chiralities is clearly revealed in the intensity difference between the equilibrium I_{eq} and chiral anomaly induced steady state I_{ca} , shown in the lower panel of Fig. 2(c).

The numerically computed ARPES spectra for a Dirac semimetal, shown in Fig. 3, similarly reveal the essential features discussed in Fig. 1. In equilibrium two bulk cones and two counterpropagating edge states at the same surface are seen in Fig. 3(a), similar to the experimental observations for Na₃Bi [13]. The nonequilibrium spectra in the presence of electric and magnetic fields are qualitatively different; two copies of the note-shaped pattern clearly reveal the chiral anomaly in Dirac semimetals. To further highlight this feature we plot, as for the Weyl semimetal, the intensity difference between the equilibrium and nonequilibrium in Fig. 3(c) for fixed $k_z = \pm 0.5$. The qualitatively most notable feature is the partial occupation of the surface state that results in the stem of the note. The bulk, though, is not entirely insensitive to the chiral anomaly: first, states are occupied up to an energy $\max(\mu_L, \mu_R)$ that is higher than in the equilibrium situation; second, only one isospin band is filled between μ_L and μ_R resulting in a decreased intensity.

Note that the surface states survive in the strong field limit when Landau levels emerge [63], but the shape of the Fermi

arc may change. A drop in the occupation along the surface states, however, remains.

D. Experimental details

From the chiral anomaly equation (3) we estimate the induced chiral chemical potential difference $\delta\mu = \mu_L - \mu_R$ to be within experimental state of the art. For the doping levels of Na₃Bi, an electric field strength of 10^4 V m⁻¹ and a magnetic field of 1 mT gives $\delta\mu$ of the order of 10 meV, which is well within ARPES resolution. Remarkably, magnetic fields as small as 6 μ T can still achieve observable $\delta\mu \approx 2.7$ meV for Na₃Bi and can reach $\delta\mu \approx 5.4$ meV in Cd₃As₂ (details of the experimental values used to compute these estimates for different materials are given in Appendix A 3, especially Table I). The fact that experimental observation of Fermi arcs in equilibrium have already been reported also bodes well [8,9,13]. To achieve momentum resolution in ARPES it is necessary to correlate the angle at which an electron is detected to its initial momentum. In free space, electrons move in straight lines making this task straightforward, and a constant electric field does not overly complicate it. A magnetic field turns the electron trajectories into spirals and may, depending on the distance to the detector and size of the magnetic field, make momentum resolution difficult. However, since the magnetic field strength needed for an observable effect is rather small, correcting induced deviations is plausible [64]. Alternatively, a larger uniform magnetic field finite within the sample could in principle be engineered with a ferromagnetic material in the picture frame geometry: a closed magnetic circuit that minimizes stray fields outside the sample that has

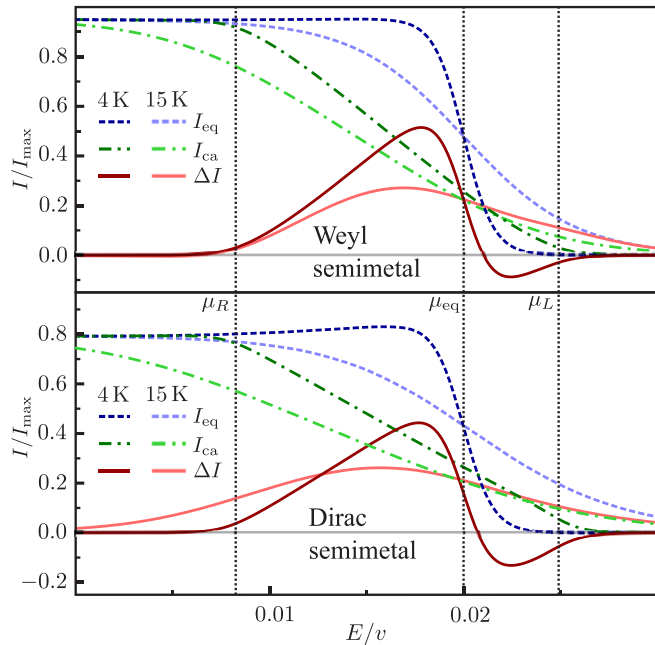


FIG. 5. Chiral anomaly in PES spectra for Dirac and Weyl semimetals. Numerically computed PES intensities for Weyl and Dirac semimetals for two different temperatures. In equilibrium the intensity I_{eq} presents a single step around μ_{eq} , that is smeared out by increasing temperature and resembles the occupation of the cones. In nonequilibrium the intensity I_{ca} shows a double-step profile with steps at μ_R and μ_L . Both $\mu_{R/L}$ include the temperature dependence of the chiral anomaly [2,21]. The difference $\Delta I = I_{\text{eq}} - I_{\text{ca}}$ highlights the effect of the chiral anomaly by a characteristic peak-dip structure for low temperatures, resulting from the shift in occupation of the two cones, that evolves into a single peak as temperature is increased. The parameters used to obtain these plots are $\mu_{\text{eq}} = 0.020v$, $\mu_L = 0.025v$, $\mu_R = 0.008v$ at 4 K and $\mu_L = 0.024v$, $\mu_R = 0.005v$ at 15 K. The temperatures are chosen to be $T = 8 \times 10^{-4}v$ and $T = 2.9 \times 10^{-3}v$, corresponding to 4 K and 15 K for a typical value of $v = 0.45$ eV. The rest of the parameters are chosen as in Figs. 2 and 3 for the upper and lower panel, respectively.

been used to experimentally study ferromagnetic metals via ARPES [65] (see Appendix A 2).

Similarly, if either field can be turned off fast enough (faster than the intervalley relaxation) a pump-probe setup could observe the nonequilibrium steady state and its equilibration, which would allow for a direct measurement of the intervalley relaxation time in addition to visualizing the chiral anomaly. While none of these are simple tasks, we believe that the rewards are significant enough that the experimental challenge will be met.

E. Case study: Na_3Bi

In order to make definite contact with current experimental state of the art, we discuss the features of the chiral anomaly for Na_3Bi . To this extent, we combine the experimental constants given in Table I with parameters obtained from *ab initio* calculations for this material that define the realistic low energy model described in Ref. [27]. Such a model is a low energy expansion of Eq. (5) that accounts for a Fermi arc curvature

via anisotropic coefficients and a topologically trivial function $\epsilon_0(\mathbf{k})$ that is even in \mathbf{k} and proportional to the identity. The equilibrium ARPES spectra computed for such model is shown in Fig. 4(a). The figure shows a clear pair of curved Fermi arcs that connect two Dirac nodes. Distinguishing clearly this pair of arcs is well within experimental resolution, as confirmed by recent experiments (cf. Fig. 2A of Ref. [13]). Upon applying external fields that satisfy $\mathbf{E} \cdot \mathbf{B} \neq 0$, the chiral anomaly induces a chiral chemical potential difference of the order $\delta\mu \sim 10$ meV, as estimated in the last section and Appendix A 3. In Fig. 4(b), we show the chiral anomaly induced ARPES spectrum for Na_3Bi corresponding to such value of $\delta\mu$. The surface states at a constant energy are partially occupied and thus end before reaching the bulk Fermi surface, the latter not visible within this resolution. The observation of such features would directly visualize the chiral anomaly and confirm its effect on the surface electronic spectrum as predicted before.

F. Absence of momentum resolution: PES

In the absence of momentum resolution the angular averaged but energy resolved photoemission spectroscopy likewise contains direct signatures of the chiral anomaly. In Fig. 5 we plot the numerically computed PES spectra as a function of energy for both Weyl and Dirac semimetals. In equilibrium it has a single step that is smeared by temperature. In the nonequilibrium steady state occupation is shifted from lower energies to higher, such that the bulk spectra would have a double step profile, with one step at μ_L and the other at μ_R . In the total spectra the two steps are hard to see since the surface states contribute significantly to smoothen the profile. The intensity difference $\Delta I = I_{\text{eq}} - I_{\text{ca}}$ instead shows a characteristic peak-dip structure for low temperatures, which reflects the chiral anomaly pumping of fermions of one chirality into the other, evolving into a single peak as temperature is increased.

III. SUMMARY AND CONCLUSION

In conclusion, we have promoted photoemission as a tool to experimentally visualize the chiral anomaly in the solid state. The main effect that allows this is the tilt of the Fermi arc in the presence of nonorthogonal electric and magnetic fields that, through the chiral anomaly, pump electrons from one chirality to the other. As a consequence, the surface state occupation at a fixed energy no longer connects bulk nodes but rather terminates in between, resulting in a qualitatively distinct note-shaped photoemission pattern identifying the chiral anomaly. We argued, by estimating from experimentally available parameters the relevant chiral chemical potential difference to be about 10 meV, that a direct visualization of the chiral anomaly is within the state of the art. Were it to be realized experimentally in the way proposed here, a revealing light would be shed on the relation between two fundamental concepts: quantum anomalies and topological states of matter.

ACKNOWLEDGMENTS

We thank Sergey Borisenko, Bernd Büchner, and Ilya Belopolski for useful discussions about Dirac semimetals and

possible extensions of current ARPES setups, and Soumya Bera for helpful insights on numerical methods.

APPENDIX: ADDITIONAL ASPECTS OF EXPERIMENTAL IMPLEMENTATION

1. Relaxation rates

The experimental feasibility of detecting the chiral anomaly with photoemission spectroscopy relies first on the correct hierarchy of the different relaxation rates involved. As discussed in the main text, for Weyl semimetals the intravalley relaxation rate at fixed chirality must be faster than the intervalley relaxation rate, $\tau_c^{-1} \gg \tau_v^{-1}$. For Dirac semimetals it is also required that the relaxation rate between the two isospins forming each Dirac node must be shorter than the intravalley relaxation, $\tau_i \gg \tau_c$. The intravalley relaxation rate τ_c can be deduced from the experimental values for the carrier mobilities μ_e given in Table I using that

$$\mu_e = \frac{\sigma}{en} = \frac{e v_F}{\hbar k_F} \tau_c, \quad (\text{A1})$$

where σ denotes the dc conductivity, e is the electric charge, and n is the carrier density. A theoretical estimate of the ratio τ_v/τ_c can be calculated in the first Born approximation following Ref. [51], rendering the values included in Table I that justify the assumptions used in the main text.

Experimentally, τ_v can be determined via nonlocal transport measurements [51]. The corresponding intervalley scattering length ℓ_v was obtained experimentally in Ref. [66] for Cd_3As_2 . This length is connected to the scattering time via $\ell_v = \sqrt{D\tau_v}$, where $D = \mu_e k_B T / e$ is the charge diffusion coefficient at temperature T . Together with mobility measurements, the intervalley scattering time τ_v at $T = 4$ K can be determined to be $\tau_v \sim 10^{-9}$ s, similar to the theoretical estimate for Na_3Bi .

2. ARPES in finite magnetic fields

ARPES experiments in magnetic fields are challenging. External magnetic fields affect electron trajectories (especially those with low energies) and compromise angle resolution. Typical ARPES equipment is protected from external magnetic fields using μ -metal shields made from a metallic alloy with high magnetic permeability μ . This material offers the magnetic field lines a path with a low magnetic resistance (or reluctance) that is inversely proportional to μ , preventing them going to the energetically costly exterior. In typical ARPES experiments, for instance the setup of Ref. [64], high resolution requires the field inside the ARPES lens to be of the order of μT or less. In practice up to $\sim 6 \mu\text{T}$ can be handled [64]. These small magnetic fields typically induce a rigid shift of the electron trajectories that can in principle be corrected [64]. As we discuss in the next section, already these small fields can result in observable values of the chiral potential difference $\delta\mu \sim 4$ meV.

To allow for measurements in larger magnetic fields, without altering electron trajectories, it would be advantageous to go one step beyond existing setups. We suggest that a possible experimental design can be based on early ideas used to perform ARPES on ferromagnetic materials [65,70]. Stray fields around ferromagnetic materials, like nickel, can severely alter photoelectron trajectories and jeopardize ARPES measurement accuracy. An elegant experimental solution studied these materials in the so-called picture frame geometry or remnant state [65,70] (see Fig. 6). In this geometry, the magnetic field lines are confined within the material in a magnetic loop, minimizing their effect on electron trajectories that can spoil ARPES measurements. To reach a uniform field within a Weyl or Dirac semimetal sample, while minimizing the external stray fields, one possible solution is to open up a small gap in the magnetic circuit as shown in Fig. 6. In this setup, a very uniform field is obtained within the gap, with possible additional fringing fields depicted as curved field

TABLE I. Summary of experimentally measured Fermi velocities v and v_z , mobilities μ_e , and theoretical estimates for the relevant scattering times. For TaAs W1 (W2) nomenclature classifies the eight (sixteen) Weyl points falling on (away) the $k_z = 2\pi/c$ plane. The scattering rate τ_c is estimated for an isotropic Weyl or Dirac cone with $E_F = \hbar v k_F \sim 10$ meV.

	Dirac semimetals				Weyl semimetal	
	Cd_3As_2	Ref.	Na_3Bi	Ref.	TaAs	Ref.
μ_e ($\text{cm}^2 \text{V}^{-1} \text{s}^{-1}$)	10^4 – 10^5	[14,19,20,67]	$\sim 10^3$ – 10^4	[68] ^a	5×10^5	[69]
τ_c (s) [Eq. (A1)]	$\sim 10^{-14}$ – 10^{-13}		$\sim 10^{-13}$		$\sim 10^{-12}$	
τ_v/τ_c [Theoretical]			10^4	[51]	500	[51]
τ_i/τ_c [Theoretical]			10^3	[51]	τ_i not defined	
τ_v (s) [Experiment]	10^{-9}	[66] ^b				
v ($\frac{\text{m}}{\text{s}}$)	7.6×10^5	[15]	3.74×10^5	[11]	$(3.1\text{--}3.6) \times 10^5$ (W1)	[41]
	9.3×10^5	[18]			$(2.6\text{--}4.3) \times 10^5$ (W2)	[41]
	1.1×10^6	[19]				
	1.3×10^6	[17]				
	1.5×10^6	[14]				
v_z ($\frac{\text{m}}{\text{s}}$)	$\sim 10^5$	[14]	2.89×10^5	[11]	3.4×10^5 (W1)	[41]
	3.3×10^5	[17]			4.1×10^4 (W2)	[41]

^aIlya Belopolski (private communication).

^bMeasurement of ℓ_v ; the intervalley relaxation time was obtained as described in the text.

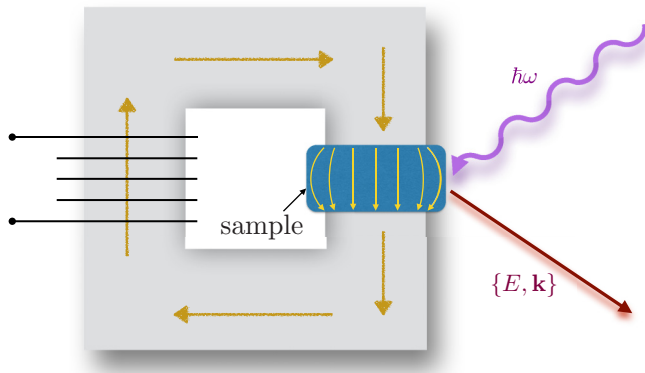


FIG. 6. Proposed magnetic circuit for studying the chiral anomaly and ARPES in a magnetic field, based on ARPES experiments on ferromagnetic materials [65]. The sample is included in a magnetic circuit to minimize stray field effects on photoelectron trajectories. The yellow arrows show the confined magnetization in the ferromagnetic material (e.g., nickel or iron) shaped into the picture-frame geometry. The Weyl or Dirac semimetal sample, a photon of energy $\hbar\omega$, and a photoelectron with energy and momentum $\{E, \mathbf{k}\}$ are depicted schematically as a blue rectangle, a purple curved arrow, and a red straight arrow, respectively.

lines. The effect of the fringing field is to increase the effective area of the gap, thus reducing its reluctance and increasing the effective magnetic field felt by the sample [71]. The magnitude and spatial extent of the fringing field can therefore be optimized by increasing the gap's length or cross section. In addition, if the sample cross section is designed to be slightly larger than the cross section of the gap, the fringing fields could enter the sample as well, not affecting photoelectron trajectories as shown in Fig. 6. Finally we note that external current loops were commonly used in experiments to orient the magnetization [65,70]. Therefore, it is plausible that these

setups can admit modifications to incorporate electric fields as well.

3. Estimates of the chiral chemical potential difference

To observe the note-shaped pattern that signals the chiral anomaly it is essential that the induced chemical potential difference $\delta\mu$ is larger than the energy resolution of the experiments, which is of the order of $\sim\text{meV}$ [72] if magnetic fields are kept of the order of $\sim\mu\text{T}$. To estimate the difference $\delta\mu = \mu_L - \mu_R$, we use the definition of the chiral chemical potentials given by Eq. (3) of the main text. For the particular case where $\mu_{\text{eq}} = 0$, this difference is given by

$$\delta\mu = 2\left(\frac{3}{2}\hbar v^2 v_z e^2 \tau_v \mathbf{E} \cdot \mathbf{B}\right)^{1/3}, \quad (\text{A2})$$

where v and v_z are the anisotropic cone Fermi velocities defined in Sec. II B of the main text and reproduced in Table I as measured by ARPES for Na_3Bi and Cd_3As_2 . From Eq. (A2) we observe that it is the magnitude of the Fermi velocities, rather than τ_v or \mathbf{B} , that can most effectively enhance the chiral anomaly.

To calculate $\delta\mu$ we choose two different magnetic field values $|\mathbf{B}| = 6\mu\text{T}$ and $|\mathbf{B}| = 1\text{mT}$. The first corresponds to a reasonable magnetic environment that can be achieved in ARPES as discussed in the previous section, while the second is a very conservative estimate of the magnetic fields that can be achieved with the frame geometry also introduced above. All our following estimates are calculated for $|\mathbf{E}| = 1 \times 10^4 \text{V m}^{-1}$. For the relaxation rates, we choose the experimentally obtained time $\tau_v = 10^{-9} \text{s}$ for Cd_3As_2 and the theoretical estimate $\tau_v/\tau_c = 10^4$ for Na_3Bi , both justified in Appendix A 1. These are also conservative estimates since τ_v is expected to be even larger for small chemical potentials [51]. Given these values, we find for Cd_3As_2 and field strengths of $|\mathbf{B}| = 1\text{mT}$ ($6\mu\text{T}$) a chiral chemical potential difference of $\delta\mu \sim 30\text{meV}$ (5.4meV). For Na_3Bi , we find that $\delta\mu \sim 15\text{meV}$ (2.7meV) for $|\mathbf{B}| = 1\text{mT}$ ($6\mu\text{T}$).

[1] R. A. Bertlmann, *Anomalies in Quantum Field Theories* (Clarendon Press, Oxford, UK, 1996).
 [2] G. E. Volovik, *The Universe in Helium Droplet* (Clarendon Press, Oxford, UK, 2003).
 [3] G. E. Volovik, *JETP Lett.* **98**, 753 (2014).
 [4] A. M. Turner and A. Vishwanath, in *Contemporary Concepts of Condensed Matter Science* (Elsevier, Amsterdam, 2013), Vol. 6. Chap. 11.
 [5] P. Hosur and X. Qi, *C. R. Phys.* **14**, 857 (2013).
 [6] H. Weng, C. Fang, Z. Fang, B. A. Bernevig, and X. Dai, *Phys. Rev. X* **5**, 011029 (2015).
 [7] S.-M. Huang, S.-Y. Xu, I. Belopolski, C.-C. Lee, G. Chang, B. Wang, N. Alidoust, G. Bian, M. Neupane, C. Zhang, S. Jia, A. Bansil, H. Lin, and M. Z. Hasan, *Nat. Commun.* **6**, 7373 (2015).
 [8] S.-Y. Xu, I. Belopolski, N. Alidoust, M. Neupane, G. Bian, C. Zhang, R. Sankar, G. Chang, Z. Yuan, C.-C. Lee, S.-M. Huang, H. Zheng, J. Ma, D. S. Sanchez, B. Wang, A. Bansil, F. Chou, P. P. Shibayev, H. Lin, S. Jia, and M. Z. Hasan, *Science* **349**, 613 (2015).

[9] B. Q. Lv, H. M. Weng, B. B. Fu, X. P. Wang, H. Miao, J. Ma, P. Richard, X. C. Huang, L. X. Zhao, G. F. Chen, Z. Fang, X. Dai, T. Qian, and H. Ding, *Phys. Rev. X* **5**, 031013 (2015).
 [10] S.-Y. Xu, C. Liu, S. K. Kushwaha, T.-R. Chang, J. W. Krizan, R. Sankar, C. M. Polley, J. Adell, T. Balasubramanian, K. Miyamoto, N. Alidoust, G. Bian, M. Neupane, I. Belopolski, H.-T. Jeng, C.-Y. Huang, W.-F. Tsai, H. Lin, F. C. Chou, T. Okuda, A. Bansil, R. J. Cava, and M. Z. Hasan, [arXiv:1312.7624](https://arxiv.org/abs/1312.7624).
 [11] Z. K. Liu, B. Zhou, Y. Zhang, Z. J. Wang, H. M. Weng, D. Prabhakaran, S.-K. Mo, Z. X. Shen, Z. Fang, X. Dai, Z. Hussain, and Y. L. Chen, *Science* **343**, 864 (2014).
 [12] S. K. Kushwaha, J. W. Krizan, B. E. Feldman, A. Gyenis, M. T. Randeria, J. Xiong, S.-Y. Xu, N. Alidoust, I. Belopolski, T. Liang, M. Zahid Hasan, N. P. Ong, A. Yazdani, and R. J. Cava, *APL Mater.* **3**, 041504 (2015).
 [13] S.-Y. Xu, C. Liu, S. K. Kushwaha, R. Sankar, J. W. Krizan, I. Belopolski, M. Neupane, G. Bian, N. Alidoust, T.-R. Chang, H.-T. Jeng, C.-Y. Huang, W.-F. Tsai, H. Lin, P. P. Shibayev, F.-C. Chou, R. J. Cava, and M. Z. Hasan, *Science* **347**, 294 (2015).

- [14] M. Neupane, S.-Y. Xu, R. Sankar, N. Alidoust, G. Bian, C. Liu, I. Belopolski, T.-R. Chang, H.-T. Jeng, H. Lin, A. Bansil, F. Chou, and M. Z. Hasan, *Nat. Commun.* **5**, 3786 (2014).
- [15] S. Borisenko, Q. Gibson, D. Evtushinsky, V. Zabolotnyy, B. Büchner, and R. J. Cava, *Phys. Rev. Lett.* **113**, 027603 (2014).
- [16] H. Yi, Z. Wang, C. Chen, Y. Shi, Y. Feng, A. Liang, Z. Xie, S. He, J. He, Y. Peng, X. Liu, Y. Liu, L. Zhao, G. Liu, X. Dong, J. Zhang, M. Nakatake, M. Arita, K. Shimada, H. Namatame, M. Taniguchi, Z. Xu, C. Chen, X. Dai, Z. Fang, and X. J. Zhou, *Sci. Rep.* **4**, 6106 (2014).
- [17] Z. K. Liu, J. Jiang, B. Zhou, Z. J. Wang, Y. Zhang, H. M. Weng, D. Prabhakaran, S.-K. Mo, H. Peng, P. Dudin, T. Kim, M. Hoesch, Z. Fang, X. Dai, Z. X. Shen, D. L. Feng, Z. Hussain, and Y. L. Chen, *Nat. Mater.* **13**, 677 (2014).
- [18] T. Liang, Q. Gibson, M. N. Ali, M. Liu, R. J. Cava, and N. P. Ong, *Nat. Mater.* **14**, 280 (2015).
- [19] L. P. He, X. C. Hong, J. K. Dong, J. Pan, Z. Zhang, J. Zhang, and S. Y. Li, *Phys. Rev. Lett.* **113**, 246402 (2014).
- [20] J. Feng, Y. Pang, D. Wu, Z. Wang, H. Weng, J. Li, X. Dai, Z. Fang, Y. Shi, and L. Lu, *Phys. Rev. B* **92**, 081306 (2015).
- [21] Q. Li, D. E. Kharzeev, C. Zhang, Y. Huang, I. Pletikoscic, A. V. Fedorov, R. D. Zhong, J. A. Schneeloch, G. D. Gu, and T. Valla, [arXiv:1412.6543](https://arxiv.org/abs/1412.6543).
- [22] S.-Y. Xu, N. Alidoust, I. Belopolski, Z. Yuan, G. Bian, T.-R. Chang, H. Zheng, V. N. Strocov, D. S. Sanchez, G. Chang, C. Zhang, D. Mou, Y. Wu, L. Huang, C.-C. Lee, S.-M. Huang, B. Wang, A. Bansil, H.-T. Jeng, T. Neupert, A. Kaminski, H. Lin, S. Jia, and M. Zahid Hasan, *Nat. Phys.* **11**, 748 (2015).
- [23] B. Q. Lv, N. Xu, H. M. Weng, J. Z. Ma, P. Richard, X. C. Huang, L. X. Zhao, G. F. Chen, C. E. Matt, F. Bisti, V. N. Strocov, J. Mesot, Z. Fang, X. Dai, T. Qian, M. Shi, and H. Ding, *Nat. Phys.* **11**, 724 (2015).
- [24] L. X. Yang, Z. K. Liu, Y. Sun, H. Peng, H. F. Yang, T. Zhang, B. Zhou, Y. Zhang, Y. F. Guo, M. Rahn, D. Prabhakaran, Z. Hussain, S. K. Mo, C. Felser, B. Yan, and Y. L. Chen, *Nat. Phys.* **11**, 728 (2015).
- [25] A. H. Castro Neto, F. Guinea, N. M. R. Peres, K. S. Novoselov, and A. K. Geim, *Rev. Mod. Phys.* **81**, 109 (2009).
- [26] S. M. Young, S. Zaheer, J. C. Y. Teo, C. L. Kane, E. J. Mele, and A. M. Rappe, *Phys. Rev. Lett.* **108**, 140405 (2012).
- [27] Z. Wang, Y. Sun, X.-Q. Chen, C. Franchini, G. Xu, H. Weng, X. Dai, and Z. Fang, *Phys. Rev. B* **85**, 195320 (2012).
- [28] Z. Wang, H. Weng, Q. Wu, X. Dai, and Z. Fang, *Phys. Rev. B* **88**, 125427 (2013).
- [29] X. Wan, A. M. Turner, A. Vishwanath, and S. Y. Savrasov, *Phys. Rev. B* **83**, 205101 (2011).
- [30] G. Xu, H. Weng, Z. Wang, X. Dai, and Z. Fang, *Phys. Rev. Lett.* **107**, 186806 (2011).
- [31] H. Nielsen and M. Ninomiya, *Phys. Lett. B* **130**, 389 (1983).
- [32] G. E. Volovik, *JETP Lett.* **70**, 1 (1999).
- [33] V. Aji, *Phys. Rev. B* **85**, 241101 (2012).
- [34] A. A. Zyuzin and A. A. Burkov, *Phys. Rev. B* **86**, 115133 (2012).
- [35] A. G. Grushin, *Phys. Rev. D* **86**, 045001 (2012).
- [36] P. Goswami and S. Tewari, *Phys. Rev. B* **88**, 245107 (2013).
- [37] C.-X. Liu, P. Ye, and X.-L. Qi, *Phys. Rev. B* **87**, 235306 (2013).
- [38] A. A. Abrikosov, *Phys. Rev. B* **58**, 2788 (1998).
- [39] D. T. Son and B. Z. Spivak, *Phys. Rev. B* **88**, 104412 (2013).
- [40] H.-J. Kim, K.-S. Kim, J.-F. Wang, M. Sasaki, N. Satoh, A. Ohnishi, M. Kitaura, M. Yang, and L. Li, *Phys. Rev. Lett.* **111**, 246603 (2013).
- [41] X. Huang, L. Zhao, Y. Long, P. Wang, D. Chen, Z. Yang, H. Liang, M. Xue, H. Weng, Z. Fang, X. Dai, and G. Chen, *Phys. Rev. X* **5**, 031023 (2015).
- [42] C. Zhang, S.-Y. Xu, I. Belopolski, Z. Yuan, Z. Lin, B. Tong, N. Alidoust, C.-C. Lee, S.-M. Huang, H. Lin, M. Neupane, D. S. Sanchez, H. Zheng, G. Bian, J. Wang, C. Zhang, T. Neupert, M. Zahid Hasan, and S. Jia, [arXiv:1503.02630](https://arxiv.org/abs/1503.02630).
- [43] J. Xiong, S. K. Kushwaha, T. Liang, J. W. Krizan, M. Hirschberger, W. Wang, R. J. Cava, and N. P. Ong, *Science* **350**, 413 (2015).
- [44] X. Yang, Y. Li, Z. Wang, Y. Zhen, and Z.-A. Xu, [arXiv:1506.02283](https://arxiv.org/abs/1506.02283).
- [45] C. Shekhar, F. Arnold, S.-C. Wu, Y. Sun, M. Schmidt, N. Kumar, A. G. Grushin, J. H. Bardarson, R. Donizeth dos Reis, M. Naumann, M. Baenitz, H. Borrmann, M. Nicklas, E. Hassinger, C. Felser, and B. Yan, [arXiv:1506.06577](https://arxiv.org/abs/1506.06577).
- [46] J. Du, H. Wang, Q. Mao, R. Khan, B. Xu, Y. Zhou, Y. Zhang, J. Yang, B. Chen, C. Feng, and M. Fang, [arXiv:1507.05246](https://arxiv.org/abs/1507.05246).
- [47] C. Zhang, C. Guo, H. Lu, X. Zhang, Z. Yuan, Z. Lin, J. Wang, and S. Jia, *Phys. Rev. B* **92**, 041203 (2015).
- [48] H. Li, H. He, H.-Z. Lu, H. Zhang, H. Liu, R. Ma, Z. Fan, S.-Q. Shen, and J. Wang, *Nat. Commun.* **7**, 10301 (2016).
- [49] K. Landsteiner, *Phys. Rev. B* **89**, 075124 (2014).
- [50] J. Zhou, H.-R. Chang, and D. Xiao, *Phys. Rev. B* **91**, 035114 (2015).
- [51] S. A. Parameswaran, T. Grover, D. A. Abanin, D. A. Pesin, and A. Vishwanath, *Phys. Rev. X* **4**, 031035 (2014).
- [52] P. Hosur and X.-L. Qi, *Phys. Rev. B* **91**, 081106 (2015).
- [53] P. E. C. Ashby and J. P. Carbotte, *Phys. Rev. B* **89**, 245121 (2014).
- [54] G. Başar, D. E. Kharzeev, and H.-U. Yee, *Phys. Rev. B* **89**, 035142 (2014).
- [55] P. Goswami, J. H. Pixley, and S. Das Sarma, *Phys. Rev. B* **92**, 075205 (2015).
- [56] J. Klier, I. V. Gornyi, and A. D. Mirlin, *Phys. Rev. B* **92**, 205113 (2015).
- [57] O. Vafek and A. Vishwanath, *Annu. Rev. Condens. Matter Phys.* **5**, 83 (2014).
- [58] P. A. M. Dirac, *Proc. R. Soc. A* **133**, 60 (1931).
- [59] The definition of the relaxation times includes energy relaxation processes at small momenta, which we assume happen on a time scale shorter than any elastic scattering.
- [60] R. V. Gorbachev, J. C. W. Song, G. L. Yu, A. V. Kretinin, F. Withers, Y. Cao, A. Mishchenko, I. V. Grigorieva, K. S. Novoselov, L. S. Levitov, and A. K. Geim, *Science* **346**, 448 (2014).
- [61] X.-L. Qi and S.-C. Zhang, *Rev. Mod. Phys.* **83**, 1057 (2011).
- [62] M. M. Vazifeh and M. Franz, *Phys. Rev. Lett.* **111**, 027201 (2013).
- [63] D. Bulmash and X.-L. Qi, [arXiv:1512.03437](https://arxiv.org/abs/1512.03437).
- [64] C. Enderlein, Ph.D. thesis, Freie Universität, Berlin, 2010.
- [65] R. Raue, H. Hopster, and R. Clauberg, *Phys. Rev. Lett.* **50**, 1623 (1983).
- [66] C. Zhang, E. Zhang, Y. Liu, Z.-G. Chen, S. Liang, J. Cao, X. Yuan, L. Tang, Q. Li, T. Gu, Y. W. Wu, J. Zou, and F. Xiu, [arXiv:1504.07698](https://arxiv.org/abs/1504.07698).

- [67] J.-P. Jay-Gerin, M. Aubin, and L. Caron, *Solid State Commun.* **21**, 771 (1977).
- [68] J. Xiong, S. Kushwaha, J. Krizan, T. Liang, R. J. Cava, and N. P. Ong, [arXiv:1502.06266](https://arxiv.org/abs/1502.06266).
- [69] C. Zhang, Z. Yuan, S. Xu, Z. Lin, B. Tong, M. Zahid Hasan, J. Wang, C. Zhang, and S. Jia, [arXiv:1502.00251](https://arxiv.org/abs/1502.00251).
- [70] M. Donath, *Surf. Sci. Rep.* **20**, 251 (1994).
- [71] T. Becherrawy, *Electromagnetism: Maxwell Equations, Wave Propagation and Emission* (John Wiley and Sons, New York, 2012).
- [72] G. Liu, G. Wang, Y. Zhu, H. Zhang, G. Zhang, X. Wang, Y. Zhou, W. Zhang, H. Liu, L. Zhao, J. Meng, X. Dong, C. Chen, Z. Xu, and X. J. Zhou, *Rev. Sci. Instrum.* **79**, 023105 (2008).